Numerical Exposure Assessment Report

SAR-NS_FCC-ISED-CE_6240552_WCH-PF30_V1.0

Customer: Molex CVS Bochum GmbH

Document Version 1.0 / 17th Jun, 2025

Author: David Schäfer

IMST GmbH
Carl-Friedrich-Gauß-Str. 2–4
47475 Kamp-Lintfort
Germany

Numerical Exposure Assessment Report

Versions[1]			
Release Date	**Nr.**	**Author**	**Comments**
17th Jun, 2025	1.0	David Schäfer	Initial version

Approval			
Name	**Job Title**	**Date**	**Signature**
David Schäfer	Preparation	17th Jun, 2025	
Jens Lerner	Review	17th Jun, 2025	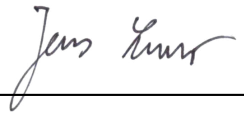

Laboratory	
Name and Address	IMST GmbH, Test Center Carl-Friedrich-Gauß-Str. 2–4 47475 Kamp-Lintfort
Accreditation	The Testcenter at IMST GmbH is a conformity assessment body (CAB) accredited by the German Accreditation Body "Deutsche Akkreditierungsstelle GmbH" (DAkkS), registered at D-PL-12139-01-00 and according to the accreditation scope D-PL-12139-01-02. It is a designated testing laboratory by the German Federal Network Agency for Electricity, Gas, Telecommunications, Post and Railway" Bundesnetzagentur" (BNetzA), registered at BNetzA-CAB-24/21-23.

Customer (Applicant / Manufacturer)		
Name and Address	Molex CVS Bochum GmbH Meesmannstr. 103 44807 Bochum, Germany Contact: Mr. Abdelnasser Farrag	Molex Technologies GmbH Mizarstraße 3 12529 Schönefeld, Germany Contact: Mr. Abdelnasser Farrag

Device Under Test (DUT)	
Type of DUT	Wireless Power Transfer Charger
Model Name	WCH-PF30
FCC ID	RK7WCH-PF30
ISED Cert. No.	4774A-WCHPF30
ISED HVIN	WCH-307b, WCH-307c, WCH-307d
Frequency Band	127.55 kHz
Active Elements	Three coils

[1] A new report revision replaces all previous versions, which hence become invalid.

Evaluation Results

Quantity inside flat phantom	Result*	Below exposure limit set by ...			
		ICNIRP	47 CFR § 1.1310	RSS-102	1999/519/EC
$SAR_{1g,\ max}$	85.5499 mW/kg	—**	Yes	Yes	—
$SAR_{10g,\ max}$	41.3143 mW/kg	Yes	Yes	Yes	Yes
$EIAV_{max}$	15.8422 V/m	Yes	—	Yes	—

*: Simulated values plus uncertainty penalties (if applicable, cf. section 3.2.5)

**: Not applicable combinations were indicated as "—"

Human Exposure Limits

Specific Absorption Rate (ICNIRP [1], 1999/519/EC [2])

Condition	Uncontrolled Environment (General Public)		Controlled Environment (Occupational)	
	SAR Limit	Mass Avg.	SAR Limit	Mass Avg.
SAR averaged over the whole body mass	0.08 W/kg	whole body	0.4 W/kg	whole body
Peak spatially-averaged SAR for the head, neck & trunk	2.0 W/kg	10 g of tissue*	10 W/kg	10 g of tissue*
Peak spatially-averaged SAR in the limbs/extremities	4.0 W/kg	10 g of tissue*	20 W/kg	10 g of tissue*
*: Defined as a tissue volume in the shape of a cube				

Specific Absorption Rate (RSS-102 Issue 6 [3])

Condition	Uncontrolled Environment (General Public)		Controlled Environment (Occupational)	
	SAR Limit	Mass Avg.	SAR Limit	Mass Avg.
SAR averaged over the whole body mass	0.08 W/kg	whole body	0.4 W/kg	whole body
Peak spatially-averaged SAR for the head, neck & trunk	1.6 W/kg	1 g of tissue*	8 W/kg	1 g of tissue*
Peak spatially-averaged SAR in the limbs/extremities	4.0 W/kg	10 g of tissue*	20 W/kg	10 g of tissue*
*: Defined as a tissue volume in the shape of a cube				

Specific Absorption Rate (47 CFR Ch. I § 1.1310 [4])

Condition	Uncontrolled Environment (General Public)		Controlled Environment (Occupational)	
	SAR Limit	Mass Avg.	SAR Limit	Mass Avg.
SAR averaged over the whole body mass	0.08 W/kg	whole body	0.4 W/kg	whole body
Peak spatially-averaged SAR	1.6 W/kg	1 g of tissue*	8 W/kg	1 g of tissue*
Peak spatially-averaged SAR for extremities, such as hands, wrists, feet, ankles, and pinnae	4.0 W/kg	10 g of tissue*	20 W/kg	10 g of tissue*
*: Defined as a tissue volume in the shape of a cube				

Internal Electric Field (ICNIRP [1], RSS-102 Issue 6 [3])

Condition	**Uncontrolled Environment** (General Public) **EIAV Limit**	**Controlled Environment** (Occupational) **EIAV Limit**
Peak EIAV @ f (in Hz)	$1.35 \cdot 10^{-4} \cdot f$ V/m	$2.7 \cdot 10^{-4} \cdot f$ V/m
Peak EIAV @ 127.55 kHz	17.2192 V/m	34.4385 V/m

Frequency Scopes

Regulation	**SAR**		**EIAV**
	local	**whole body**	
ICNIRP	100 kHz – 6 GHz	100 kHz – 300 GHz	100 kHz – 10 MHz
47 CFR § 1.1310	100 kHz – 6 GHz		—*
RSS-102 Issue 6	100 kHz – 6 GHz		3 kHz – 10 MHz
1999/ 519/EC	100 kHz – 10 GHz		—
*: Not applicable combinations were indicated as "—"			

Contents

List of Figures

List of Tables

1 Introduction

1.1 Objective

The objective is the numerical exposure assessment of one Wireless Power Transfer (WPT) charger (further referred to as "device under test" or "DUT") designed by Molex CVS Bochum GmbH (further referred to as "customer"). In particular the Specific Absorption Rate (SAR, thermal hazard) and the internal electric field (EIAV[2], instantaneous nerve stimulation hazard) were investigated and compared to the exposure limits specified by ICNIRP [1], FCC [4], ISED [3] and EUCO [2].

1.2 Simulation Method

All simulations were done with the Finite Difference Time Domain (FDTD) simulation tool Empire XPU [5]. A numerical model of the DUT was generated and validated by measurements of the magnetic field in its vicinity and measured inductance of the charging coil. The SAR and EIAV inside a flat phantom (human body part model) was investigated similar to the assessment procedures described in IEC/IEEE 62704-1 [6, 7]. The procedures were adapted to make them suitable for the low frequency of the DUT.

1.3 DUT Description

The 15 W, triple coil, wireless power charger "WCH-PF30" (further referred to as "device under test" or "DUT") can be used to charge portable devices like smart-phones (further referred to as "WPT receiver"). It is designed to be integrated into a vehicle, e.g. into the center console of a car. The DUT operates at a frequency of 127.55 kHz and features three charging coils. During operation only one of the three coils is excited/charging at a time. Which coil is used for charging is chosen by the DUT itself, depending on the placement of the WPT receiver device. A photo of the DUT is depicted in Figure 1 and a technical drawing including the DUTs dimensions is shown in Figure 2.

In addition to the "lead variant" (WCH-PF30) there are three other variants of the DUT designed for distinct mounting positions within the vehicle:

1. WCH-307b (Driver variant)
2. WCH-307c (Front and rear right passenger variant)
3. WCH-307d (Rear left passenger variant)

As outlined in the document "2.1_WCH-PF30_Difference_document_1.0.pdf" provided by the customer the four variants have different population schemes of the main/bottom PCB, the dielectric housing of the WCH-307c variant has a differently located pin ("poka-yoke" feature) to prevents its accidental installation in the wrong console slot and they run different software/firmware versions. It

[2] EIAV is the particular name of the post-processing/visualisation feature in Empire XPU. The averaging is optional and was disabled for this investigation.

Figure 1: Photo of the DUT

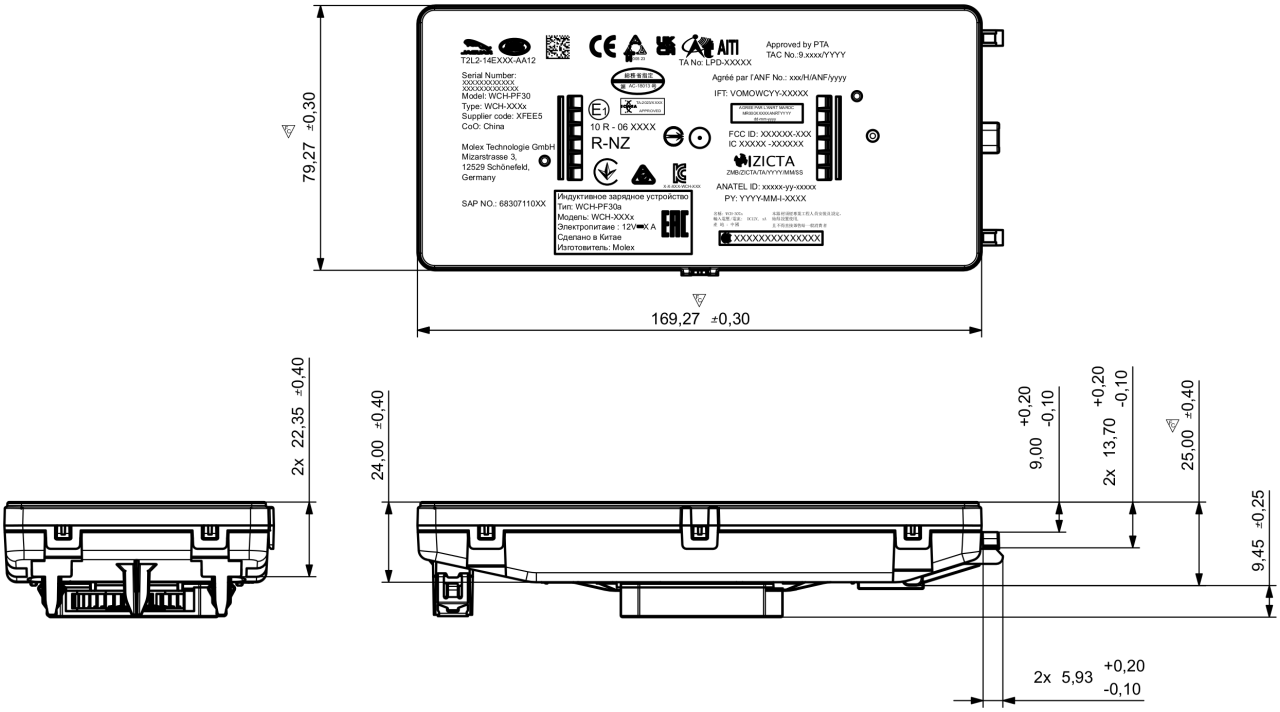

Figure 2: Excerpt of a technical drawing of the DUT, provided by the customer.

is expected that these differences will have only a minor impact on the assessed exposure quantities due to the following factors:

1. The components are situated on the bottom side of the main/bottom PCB, away from the charging coils (cf. Figure 8)
2. The main/bottom PCB components are covered by a metallic shielding
3. The dielectric parts have minimal influence on EM-fields at the low operating frequency of $127.55\,\mathrm{kHz}$
4. The different software/firmware versions are not relevant, because the numerical exposure assessment is done for a predetermined fixed coil current (cf. Section 1.4)

Therefore the different variants were not assessed individually, but only one (simplified) numerical model resembling the lead variant was investigated.

1.4 Setup for Reference Measurement

A validation of the numerical model was carried out by comparing the simulated magnetic field in the vicinity of the DUT with reference measurements. Preliminary measurements of the magnetic field showed that the worst-case configuration is given when the side coil Nr. 3 (opposite from connector) is excited, so only this operation state was considered. The measurements were executed with a series production equivalent device, running in a testing operating mode at a fixed coil current of $4.5\,\mathrm{A}$ (RMS). The customer predetermined that this is the maximum anticipated coil current, which occurs while charging a WPT receiver. During the other possible operating state of "surface observation" this coil current is not exceeded. The value is the RMS value of the coil currents complete time domain signal, not just the RMS value of the operating frequency component ($127.55\,\mathrm{kHz}$). No WPT receiver was present during the reference measurements of the magnetic field. The measurements were done on the behalf of the customer by the lab of "cetecom advanced GmbH" with the setup depicted in Figure 3. They used a SPEAG "DASY8" positioner system (cf. Figure 3a) and a "MAGPy-8H3D+E3D" field probe featuring "eight isotropic $1\,\mathrm{cm}^2$-H-field sensors, arranged at the corners of a 22 mm cube" (cf. Figure 3d). The first/lowest H-field sensor plane consisting of four H-field-sensors is located $7.5\,\mathrm{mm}$ from the probe tip. The field probe was positioned above the xy-center of the charging coil, i.e. above the charging coil axis, whereby an offset was applied to locate two of the eight H-field-sensors in the axis of the charging coil. A line measurement of the magnetic field strength was performed by lifting the probe upwards along the coil axis to different z-distances from the DUT. Figure 3b shows the lowest possible position of the field probe (touch position) with $z = 1.0\,\mathrm{mm}$ clearance, hence locating one of the four bottom H-field-sensors at $x = -14\,\mathrm{mm}$, $y = 0\,\mathrm{mm}$ and $z = 8.5\,\mathrm{mm}$. The H-field values obtained with this particular bottom H-field-sensor were used as reference measurements for the simulation, as provided in the measurement report named "1-7639-24-01-02_TR1-R04.pdf" from "2025-01-02".

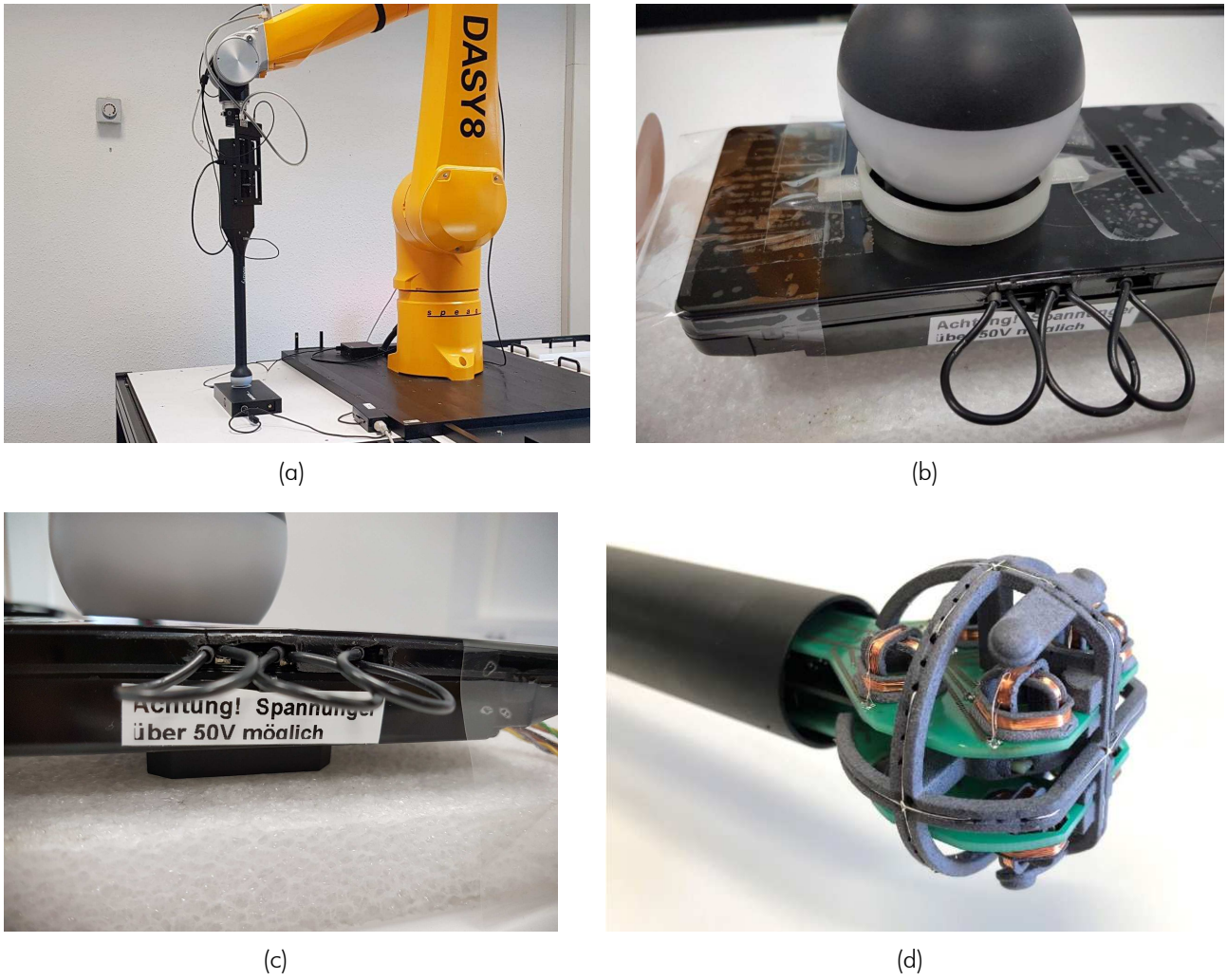

(a) (b)

(c) (d)

Figure 3: Measurement setup from the external lab of "cetecom advanced GmbH", showing (a) the SPEAG "DASY8" positioner with equipped "MAGPy-8H3D+E3D" probe, (b) and (c) the "MAGPy-8H3D+E3D" probe in touch position xy-centered over DUT coil and (d) a close-up of the "MAGPy-8H3D+E3D" probe insides. The depicted photos were taken from the measurement report and the measurement system manual.

2 EM Simulation Model

2.1 Model Setup

The simulation model of the DUT is based on STEP CAD data and ODB++ layout data provided by the customer. The data was imported into Empire XPU and then rotated and moved so that the point of intersection between the middle charging coil axis and the DUTs top side is located in the origin of the coordinate system. Figure 4 shows a top and bottom 3D view of the simulation model.

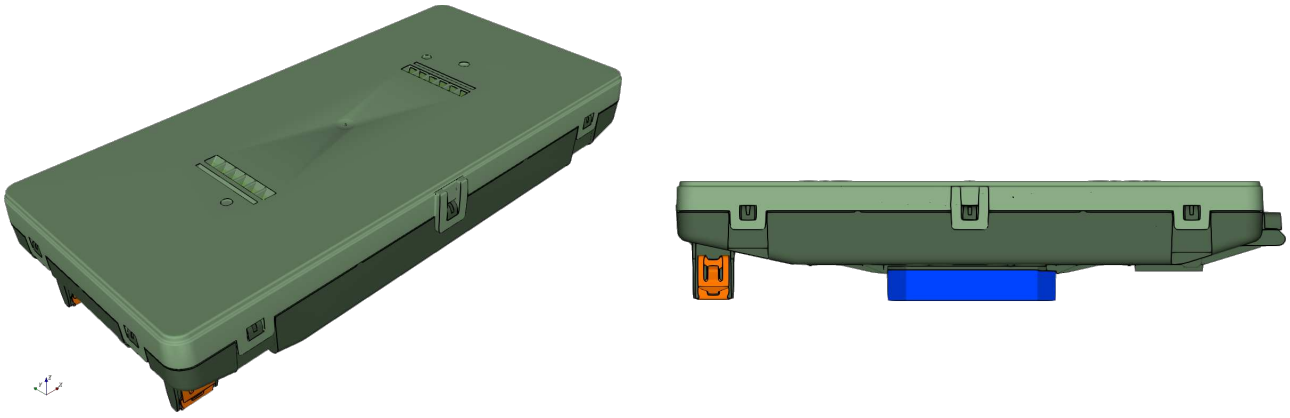

(a) (b)

Figure 4: Geometry of the Empire simulation model of the DUT, showing the outer 3D trimetric view (a) and side view (b).

In Figure 5 the internal components are visible, including the three WPT charging coils. The investigated side coil Nr. 3 can be seen in green. It has 12 turns and its middle point is located at $x = -14\,\text{mm}$, $y = 0\,\text{mm}$, $z = -5.138\,\text{mm}$ and the top side of the DUT housing is at $z = 0\,\text{mm}$.

Figure 6 and 7 show geometrical details of the simulation ports and the WPT coils.

Figure 8 shows an exploded view of the most important components of the simulation model. Based on the customers information the material properties were set as follows:

(a) DUTs top housing (PC+ABS, Bayblend FR3010, TPE Kraiburg TC6CEZ, $\epsilon_r = 3.1$)
(b) Top PCB (Copper traces, $\sigma = 59.6 \cdot 10^6\,\text{S/m}$)
(c) Coil frame (PC+ABS, Bayblend FR3010, $\epsilon_r = 3.1$)
(d) WPT coils (Copper, $\sigma = 59.6 \cdot 10^6\,\text{S/m}$)
(e) Ferrite (Mn-Zn, BP40, $\mu_r = 2300$, $tan(\delta) = 0.01$)
(f) Adhesive (UB-510, $\epsilon_r = 2.9401$)
(g) Bottom PCB (Copper traces, $\sigma = 59.6 \cdot 10^6\,\text{S/m}$; PEC components with population scheme similar to lead variant, $\sigma = inf$)
(h) Bottom PCB shielding (1.0372 steel, $\sigma = 1.45 \cdot 10^6\,\text{S/m}$)
(i) Bottom housing (PC+ABS, Bayblend FR3010, TPE Kraiburg TC6CEZ, $\epsilon_r = 3.1$)
(j) Fan dielectric/metal parts (PBT+30GF, $\epsilon_r = 3.5$ and AISI 1018, $\sigma = 3.5 \cdot 10^6\,\text{S/m}$)
(k) Clips (EN 10132-4, $\sigma = 1.45 \cdot 10^6\,\text{S/m}$)

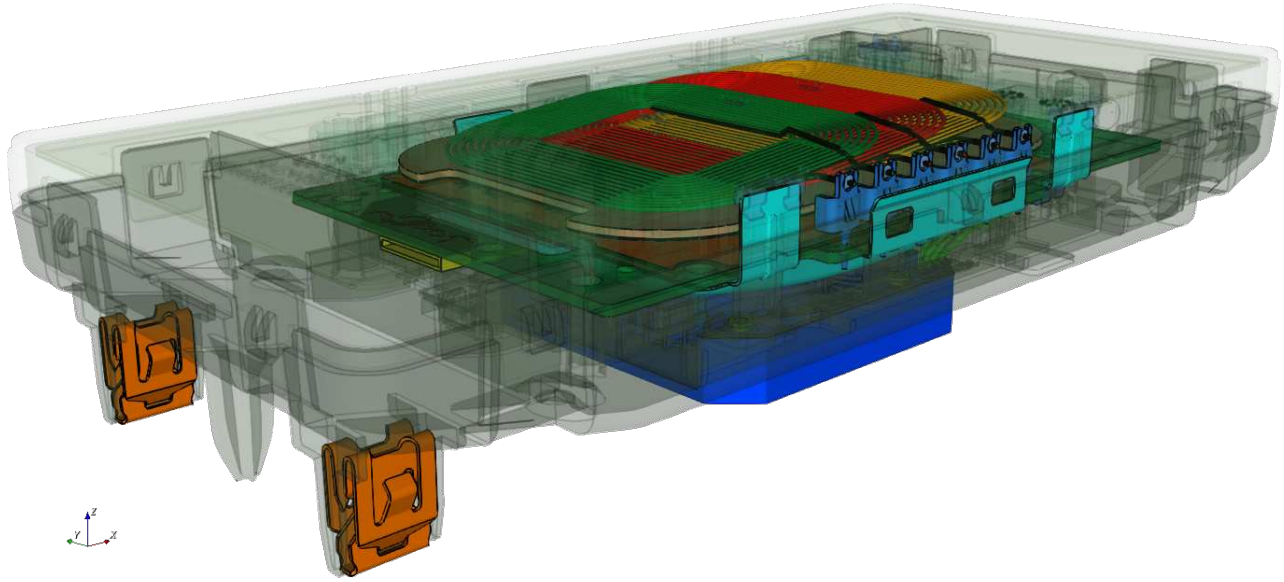

Figure 5: Geometry of the Empire simulation model of the DUT. The housing of the DUT is set transparent to show the internal components.

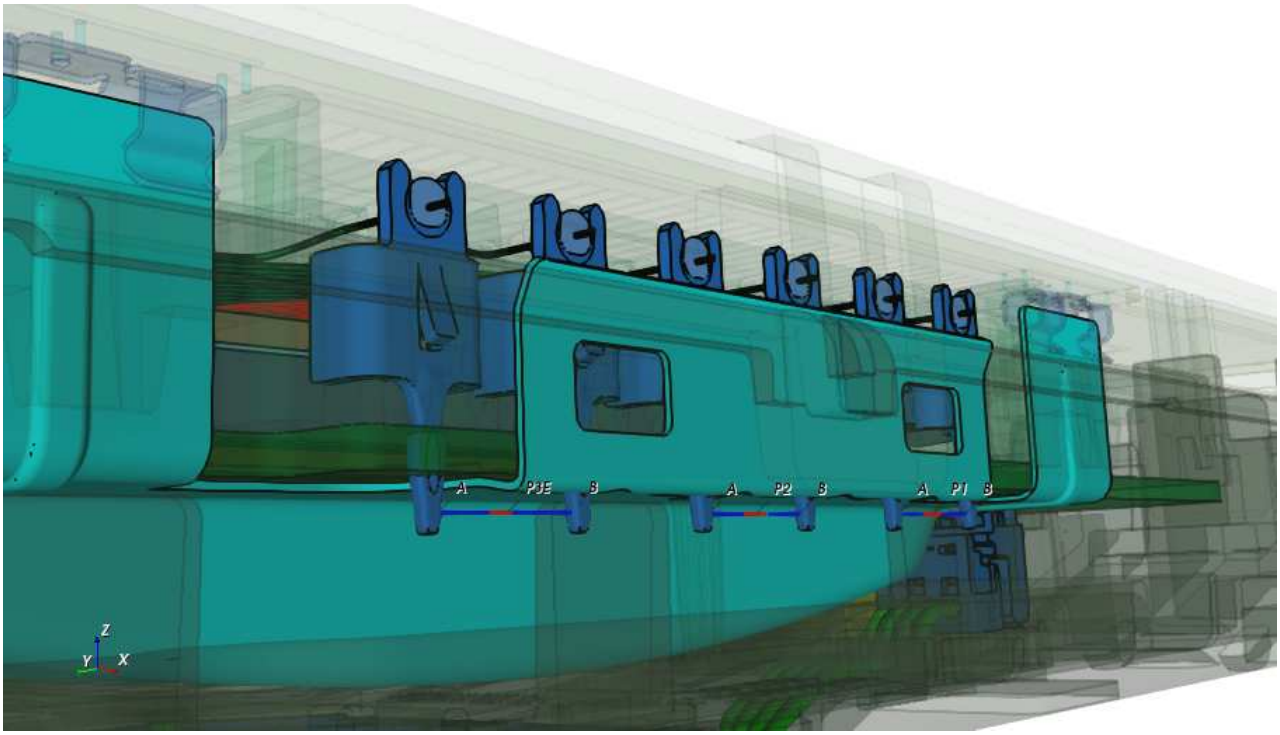

Figure 6: Geoemetry of the simulation ports. The ports were added below and close to the main PCB and small parts of the main PCB traces were cut away to prevent short circuit over the PCB.

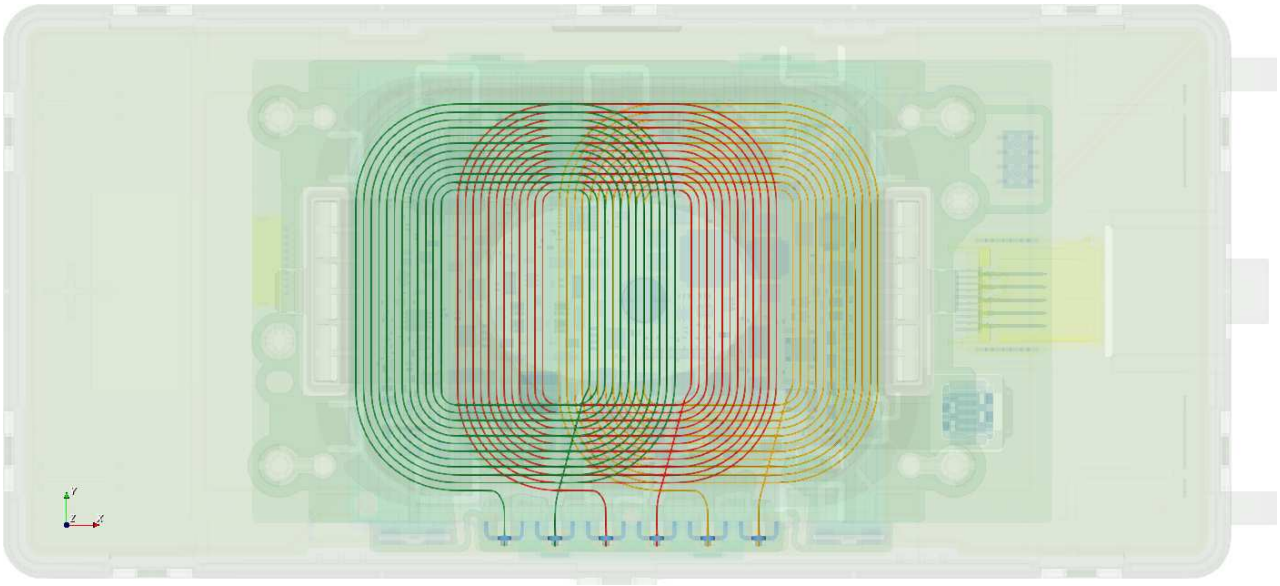

(a)

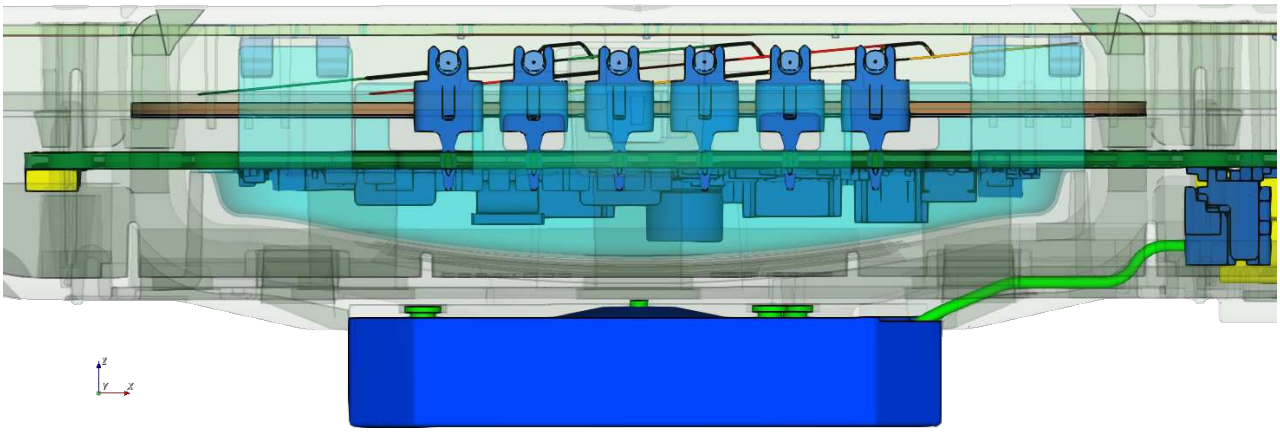

(b)

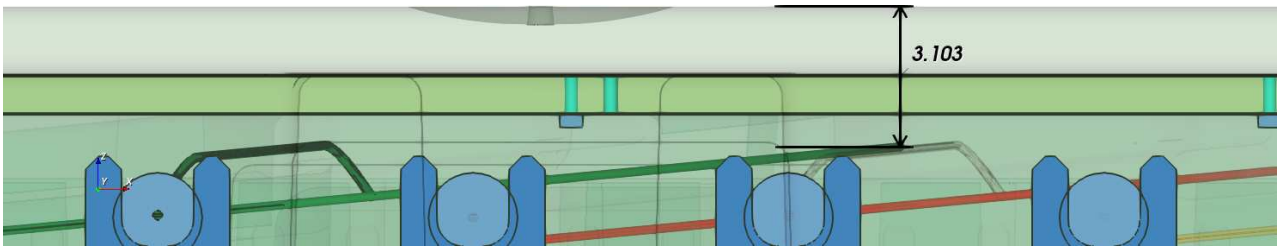

(c)

Figure 7: Geometry of the WPT charging coils in top (a) and side view (b). Each of the three coils has 12 turns. They are arranged with a subsequent overlap realized by a tilt angle of about $5.3°$. The minimum distance between the wire core (center line) and the top side of the DUT housing is about 3.1 mm (c).

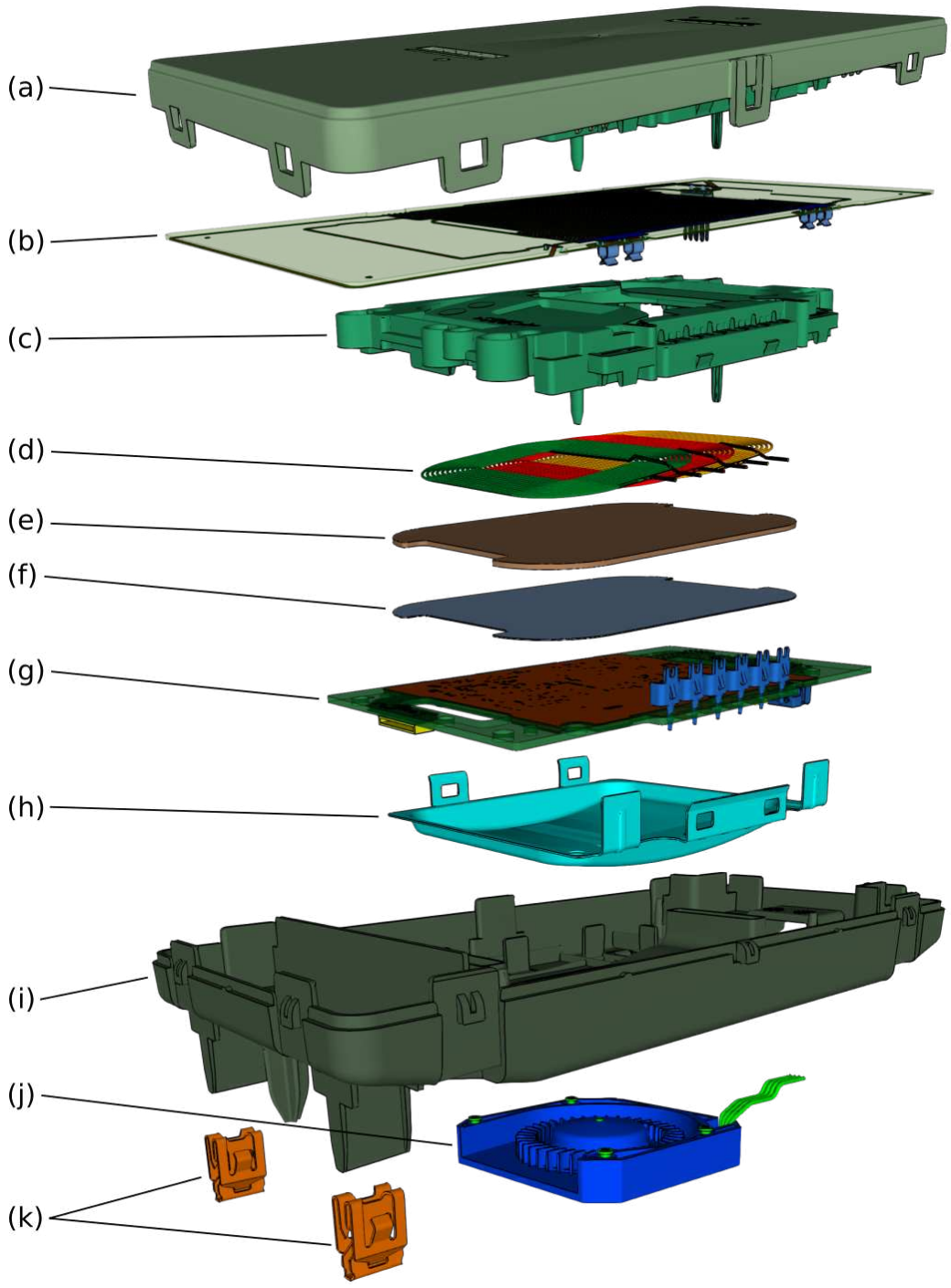

Figure 8: Geometry of the Empire simulation model of the DUT, showing an exploded view of the DUTs top housing (a), top PCB (b), coil frame (c), WPT coils (d), ferrite (e), adhesive (f), bottom PCB (g), bottom PCB shielding (h), bottom housing (i), fan/blower (j) and clips (k).

When the DUT is installed in a vehicle it is combined with an air grid, which is added on top of the DUTs housing as shown in Figure 9. The air grid allows air to pass by the bottom side of WPT receivers, cooling them during charging. Different variations of air grids can be combined with the DUT, depending on its mounting position inside the vehicle. The air grid is part of the vehicle and is not intended to be removed or exchanged by the user of the DUT. The thinnest variant was added to the numerical model which corresponds to the smallest possible separation distance and hence the strongest exposure. Its material was set to TPE ($\epsilon_r = 4.6$). The air grid was not present during the reference measurements, as can be seen from in Figure 3 in section 1.4.

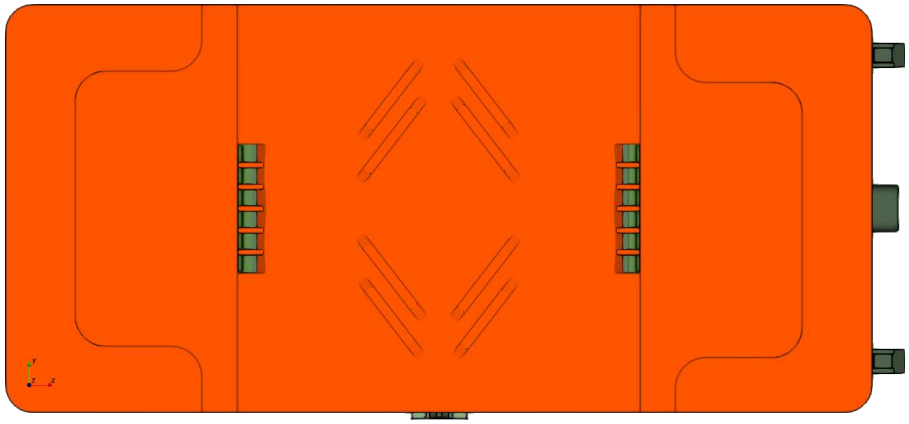

(a)

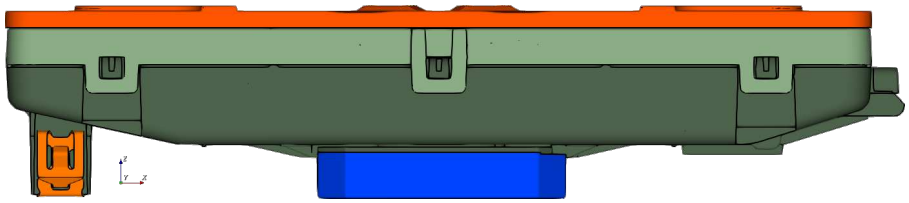

(b)

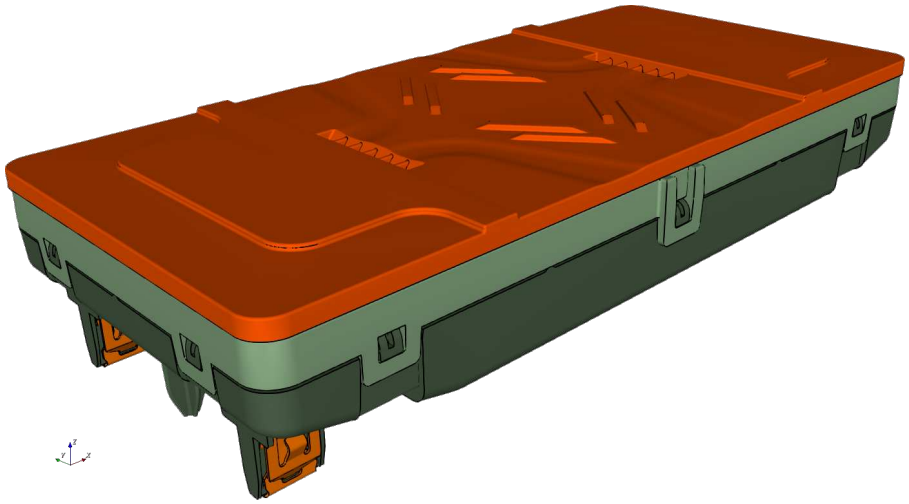

(c)

Figure 9: Geometry of the air grid (rubber mat) which was added on top of the DUT.

2.2 Model Check

The simulation model was checked by comparing the simulated magnetic fields with the reference measurement (cf. section 1.4). During measurement and simulation the charging coil was excited with the maximum expectable current of $4.5\,\mathrm{A}$ (RMS) at a frequency of $127.55\,\mathrm{kHz}$. The simulation setup was unperturbed, meaning that it didn't include a WPT receiver device or phantom (human body model).

2.2.1 Magnetic Fields

Figure 10 shows a xz-cutplane for the simulated magnetic field strength through the center of the DUT. The colour legend is logarithmic with an 70 dB range. It can be seen how the main PCBs ground and the ferrite confine the main part of the magnetic field to the dedicated WPT receiver location above the DUT.

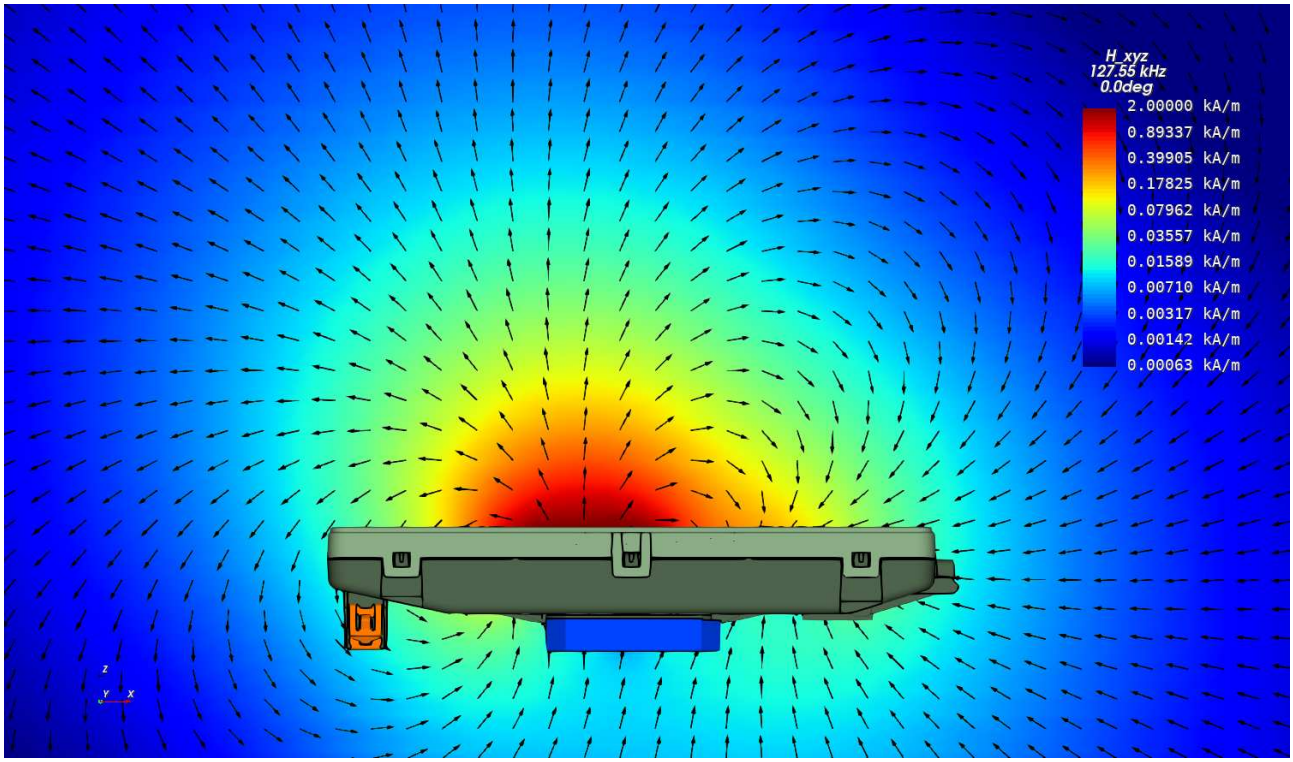

Figure 10: The simulated magnetic field displayed on a xz-plane through the DUT.

Analogue to the setup of the measurement (cf. section 1.4) the simulated magnetic field (H-field) strength was evaluated along the axis of the charging coil (side coil Nr. 3). The simulated line starts at $z = 0\,\mathrm{mm}$ which corresponds to the top of the DUTs housing. The measured line starts at $z = 8.5\,\mathrm{mm}$, so as close to the DUT as possible with respect to the necessary clearance and the "sensor center to tip distance" of the "MAGPy-8H3D+E3D" field probe (cf. section 1.4). As Table 1 and Figure 11 show, the simulated H-field is in agreement with the measurement.

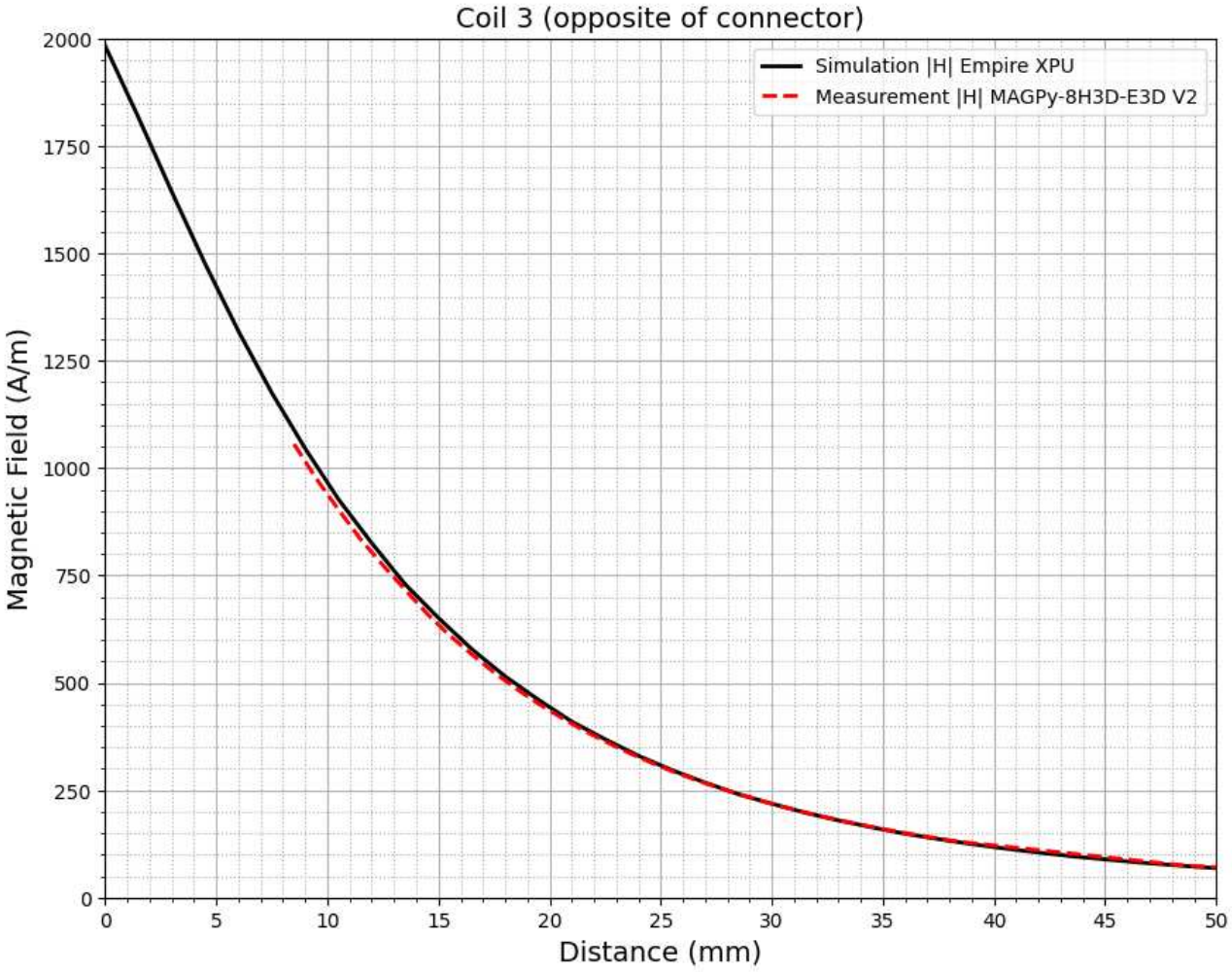

Figure 11: Curves for the line evaluation of the H-field (RMS values). The top of the DUT dielectric housing is located at $z = 0\,\text{mm}$.

z (mm)	Measurement (A/m)	Empire (A/m)
8.5	1055.99	1088.76
9.5	975.39	1006.14
10.5	903.03	927.25
11.5	833.66	859.16
12.5	773.81	793.25
13.5	716.56	729.54
14.5	660.23	677.15
15.5	610.38	626.75
16.5	566.15	578.36
17.5	524.16	536.10
18.5	486.30	496.77
19.5	451.24	460.38
20.5	419.72	426.54
21.5	389.86	395.91
22.5	363.47	368.46
23.5	338.34	342.84
24.5	315.58	318.94
25.5	294.31	296.75
26.5	275.36	277.34
27.5	257.31	258.63
28.5	240.86	240.62
29.5	225.48	225.87
30.5	211.32	211.55
31.5	198.11	197.66
32.5	186.27	185.62
33.5	174.84	174.24
34.5	164.48	163.51
35.5	154.78	153.59
36.5	145.79	144.47
37.5	137.36	136.15
38.5	129.71	128.28
48.5	74.98	73.83
58.5	46.60	45.38

Table 1: Tabular data of the measurement results shown in Figure 11 and the simulation results evaluated at the measurement locations.

2.2.2 Coil Inductance

In addition to the magnetic fields also the inductance of the coil was used to check the simulation model. With a relative deviation of $-5.58\,\%$ (cf. Table 2) the simulated inductance is in good agreement with the value from the data sheet.

	Data Sheet	Empire	Deviation
Coil Inductance	$11.500\,\mu\text{H} \pm 10\,\%$	$10.859\,\mu\text{H}$	$-5.58\,\%$

Table 2: Data sheet and simulated inductance.

2.2.3 Conclusion of Model Check

It can be concluded, that simulated magnetic field strength and inductance are in agreement (cf. Figure 11 and Table 2) with the measurements from the external lab of "cetecom advanced GmbH" and the data sheet value, indicating the accurate setup of the Empire simulation model.

3 SAR and EIAV Evaluation

For the evaluation of the Specific Absorption Rate (SAR) and the internal Electric field (EIAV) a box shaped flat phantom was added to the simulation model. The setup resembles the situation of someone touching the DUT just after a receiver removal which was in "charging mode" at maximum field. For the SAR evaluation the coil current could have been reduced according to the search mode duty cycle, but with respect to EIAV the continuous maximum expectable coil current was retained throughout the investigation.

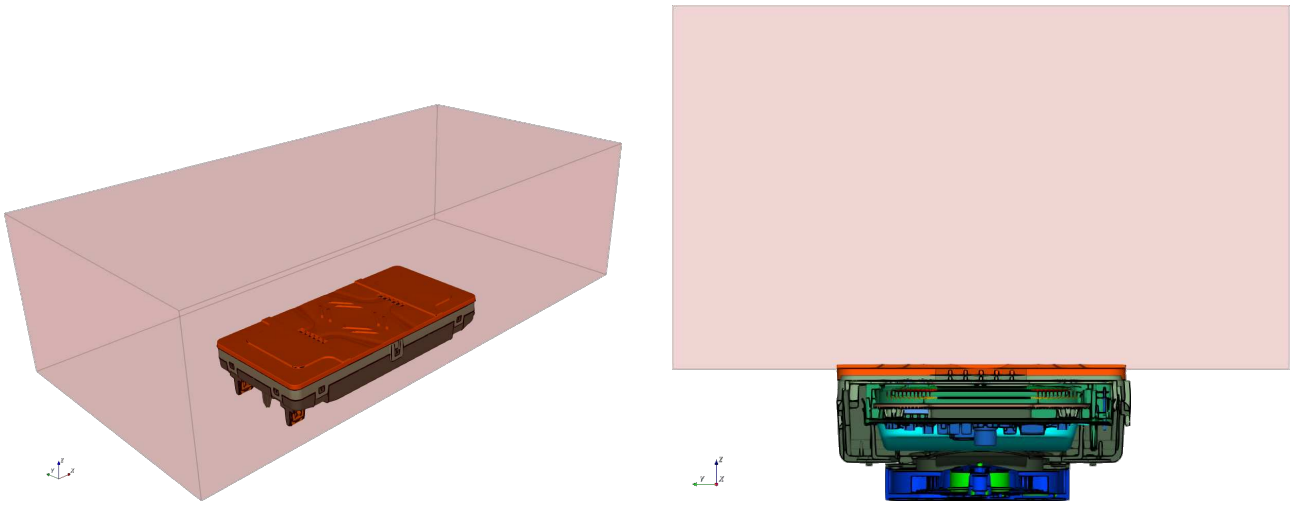

(a) (b)

Figure 12: Geometry of the flat phantom in 3D trimetric view (a) and side view (b) with the DUT model cut in half. The phantom was brought down to the lowest reachable parts of the air grid, i.e. the bottom of its recesses.

The size of the phantom was larger than twice the outer dimensions of the DUT (without air grid). The phantom was centered (xy-direction) above the center coil at closest possible z—distance, virtually touching the lowest reachable parts of the air grid, i.e. the bottom of its recesses, as shown in Figure 12 (b). This locates the phantoms bottom side (towards DUT) at $z = 1.700\,\text{mm}$. The phantoms material properties were set to the values given in RSS-102.NS.SIM [8] and IEC/IEEE 62209-1528 [9]. The following list concludes the most relevant phantom properties:

1. Geometric size: $d_x \cdot d_y \cdot d_z = 360\,\text{mm} \cdot 170\,\text{mm} \cdot 100\,\text{mm}$
2. Location of bottom side (towards DUT): $z = 1.7\,\text{mm}$
3. Relative permittivity: $\epsilon_r = 55$
4. Electrical conductivity: $\sigma = 0.75\,\text{S/m}$
5. Mass density: $\rho = 1000\,\text{kg/m}^3 = 1\,\text{g/cm}^3$

More details about the numerical model, like e.g. domain size, time step or total number of mesh cells, can be found in the appendix in section 4.1.

3.1 Simulation Results

Figure 13 and 14 show the simulated 1g- and 10g-averaged SAR and Figure 15 shows the simulated un-averaged EIAV. Table 3 lists the corresponding maximum values and their positions.

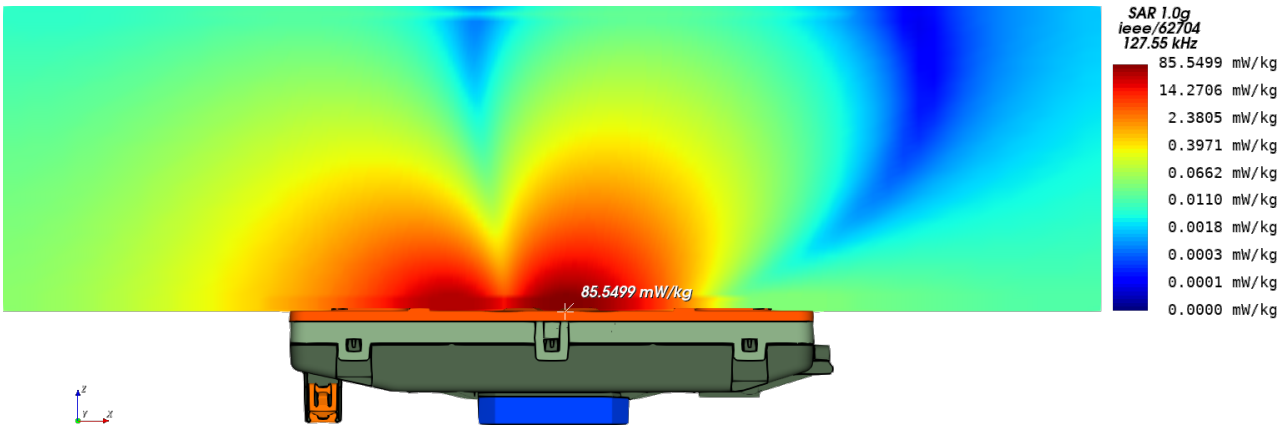

Figure 13: Cutplanes through the maxima of the simulated 1g-averaged SAR inside the flat phantom. The phantom geometry is not visible. The discontinuities at the phantom boundaries are caused by the averaging algorithm (cf. [6, Section 6.2.2]).

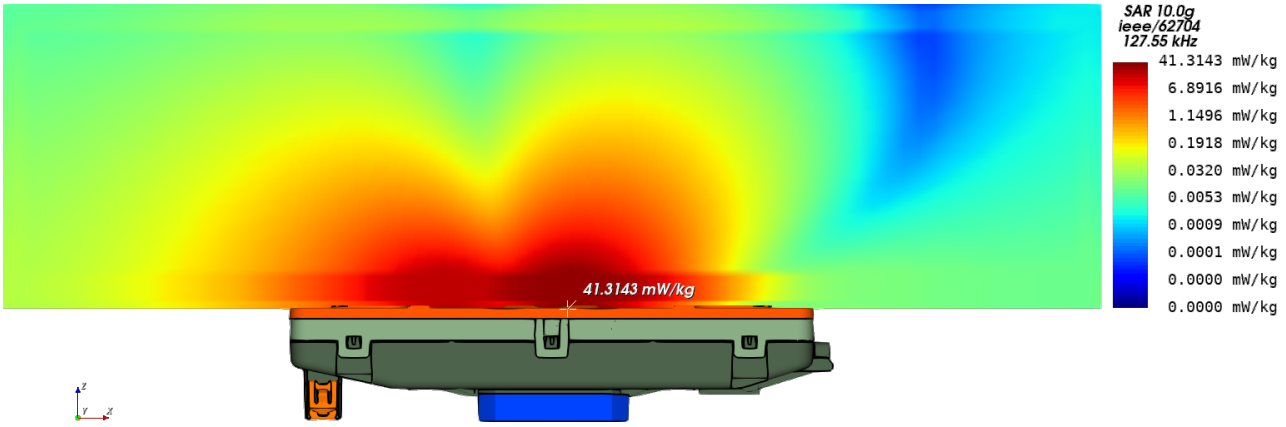

Figure 14: Cutplanes through the maxima of the simulated 10g-averaged SAR inside the flat phantom. The phantom geometry is not visible. The discontinuities at the phantom boundaries are caused by the averaging algorithm (cf. [6, Section 6.2.2]).

Quantity	Maximum Value	Position of Maximum		
		x	y	z
$SAR_{1g,\,max}$	85.5499 mW/kg	4.389 mm	−0.216 mm	1.829 mm
$SAR_{10g,\,max}$	41.3143 mW/kg	5.328 mm	−0.216 mm	1.829 mm
$EIAV_{unaveraged,max}$	15.8422 V/m	3.927 mm	−0.216 mm	1.829 mm

Table 3: SAR and EIAV maximum values with their corresponding positions.

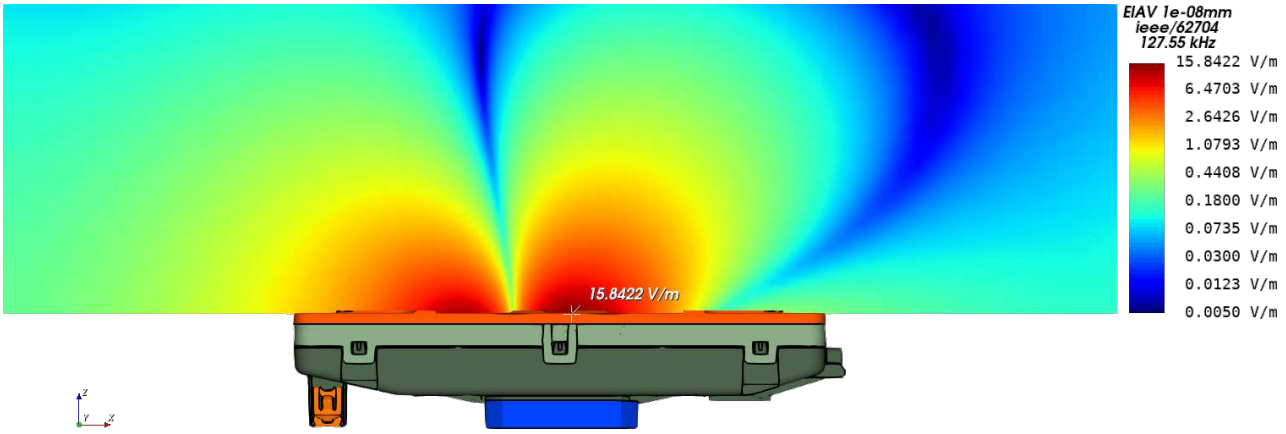

Figure 15: Cutplane through the maximum of the simulated EIAV inside the flat phantom. The phantom geometry is not visible.

3.2 Simulation Uncertainty

Based on chapter 7 of IEC/IEEE 62704-1 [6] the Combined- and Expanded Standard Uncertainty was calculated to analyse the accuracy of the results for the numerical model (further referred to as "reported model"). Because the DUTs operating frequency is below the scope of the standard, the procedure had to be modified. Details about this will be described in the following sections.

3.2.1 Simulation Parameter Related Uncertainty

The procedure for evaluating the simulation parameter related uncertainty (IEC/IEEE 62704-1 [6, section 7.2]) was modified as described in Table 4. Table 5, 6, 7 and 8 show the maximum SAR and EIAV for the investigated variants as well as their relative deviation from the reported model. Table 9, 10 and 11 show the budget of the SAR and EIAV uncertainty contributions of the simulation parameters.

Uncertainty Component	Applicability of the Procedure from IEC/IEEE 62704-1 [6, section 7.2]	Nr. of Variations
Positioning	Applicable. The distance between phantom and DUT was increased by +1 mesh step	1
Mesh Resolution	Not 1:1 applicable. Requested refinement is not practicable at 127.55 kHz. Instead, total number of mesh cells was increased by a factor of 2	1
Boundary Condition	Not 1:1 applicable, because $\lambda/4$ (=587.598 m) is way too large at 127.55 kHz. Instead, simulation domain was enlarged by 50% simultaneously in +/- x/y/z direction	1
Power Budget	Not applicable. No travelling wave conditions are given, so comparison with power absorbed in ABC is not possible. Excitation will be normalized to fixed port/coil current.	0
Convergence	Not 1:1 applicable. Instead it was simulated longer by a factor of (at least) 1.5 more time steps.	1
Phantom dielectrics	Not applicable / not indicated because fixed permittivity and conductivity from [8, 9] were used.	0

Table 4: Description of the modified procedure for obtaining the uncertainty budget.

Phantom z-Position	1.700 mm	1.950 mm
$SAR_{1g,\,max}$	85.5499 mW/kg	82.1151 mW/kg
$SAR_{10g,\,max}$	41.3143 mW/kg	39.8238 mW/kg
$EIAV_{max}$	15.8422 V/m	15.4781 V/m
$SAR_{1g,\,max}$-Deviation	0 %	−4.01 %
$SAR_{10g,\,max}$-Deviation	0 %	−3.61 %
EIAV-Deviation	0 %	−2.30 %

Table 5: SAR and EIAV results for different phantom positions. The first data column corresponds to the reported model (cf. section 3.1).

Mesh Resolution	8.462 MCells	19.372 MCells
$SAR_{1g,\,max}$	85.5499 mW/kg	85.4331 mW/kg
$SAR_{10g,\,max}$	41.3143 mW/kg	41.0694 mW/kg
$EIAV_{max}$	15.8422 V/m	15.9559 V/m
$SAR_{1g,\,max}$-Deviation	0 %	−0.14 %
$SAR_{10g,\,max}$-Deviation	0 %	−0.59 %
EIAV-Deviation	0 %	0.72 %

Table 6: SAR and EIAV results for different mesh resolutions. The first data column corresponds to the reported model (cf. section 3.1). To compensate for the smaller FDTD timestep the simulation time was increased to 2.012 Msteps.

Domain Size	660 mm · 488 mm · 416 mm	1320 mm · 976 mm · 832 mm
$SAR_{1g,\,max}$	85.5499 mW/kg	85.5851 mW/kg
$SAR_{10g,\,max}$	41.3143 mW/kg	41.3342 mW/kg
$EIAV_{max}$	15.8422 V/m	15.8458 V/m
$SAR_{1g,\,max}$-Deviation	0 %	0.04 %
$SAR_{10g,\,max}$-Deviation	0 %	0.05 %
EIAV-Deviation	0 %	0.02 %

Table 7: SAR and EIAV results for different simulation domain sizes. The first data column corresponds to the reported model (cf. section 3.1). The simulation domain was enlarged symmetrically in all spatial directions.

Time Steps	1.0 MSteps	2.0 MSteps
Energy Decay	−98.0 dB	−100.9 dB
$SAR_{1g,\,max}$	85.5499 mW/kg	86.4684 mW/kg
$SAR_{10g,\,max}$	41.3143 mW/kg	41.7707 mW/kg
$EIAV_{max}$	15.8422 V/m	15.9266 V/m
$SAR_{1g,\,max}$-Deviation	0 %	1.07 %
$SAR_{10g,\,max}$-Deviation	0 %	1.10 %
EIAV-Deviation	0 %	0.53 %

Table 8: SAR and EIAV results for different number of total time steps. The first data column corresponds to the reported model (cf. section 3.1).

Uncertainty Component	Section in [6]	1g-SAR Tolerance in %	Probability Distribution	Divisor	c_i	1g-SAR Uncertainty in %
Positioning	7.2.1	$-4.01\,\%$	R	1.73	1	$-2.32\,\%$
Mesh Resolution	7.2.2	$-0.14\,\%$	N	1	1	$-0.14\,\%$
Boundary Condition	7.2.3	$0.04\,\%$	N	1	1	$0.04\,\%$
Power Budget	7.2.4	*not appl.*	N	1	1	*not appl.*
Convergence	7.2.5	$1.07\,\%$	R	1.73	1	$0.62\,\%$
Phantom dielectrics	7.2.6	*not appl.*	R	1.73	1	*not appl.*
Combined Std. Uncertainty (k=1)						$2.41\,\%$

Table 9: Budget of the 1g-SAR uncertainty contributions of the simulation parameters, corresponding to IEC/IEEE 62704-1 [6, Table 3]. Note: N, R, U = normal, rectangular, U-shaped probability distributions.

Uncertainty Component	Section in [6]	10g-SAR Tolerance in %	Probability Distribution	Divisor	c_i	10g-SAR Uncertainty in %
Positioning	7.2.1	$-3.61\,\%$	R	1.73	1	$-2.09\,\%$
Mesh Resolution	7.2.2	$-0.59\,\%$	N	1	1	$-0.59\,\%$
Boundary Condition	7.2.3	$0.05\,\%$	N	1	1	$0.05\,\%$
Power Budget	7.2.4	*not appl.*	N	1	1	*not appl.*
Convergence	7.2.5	$1.10\,\%$	R	1.73	1	$0.64\,\%$
Phantom dielectrics	7.2.6	*not appl.*	R	1.73	1	*not appl.*
Combined Std. Uncertainty (k=1)						$2.26\,\%$

Table 10: Budget of the 10g-SAR uncertainty contributions of the simulation parameters, corresponding to IEC/IEEE 62704-1 [6, Table 3]. Note: N, R, U = normal, rectangular, U-shaped probability distributions.

Uncertainty Component	Section in [6]	EIAV Tolerance in %	Probability Distribution	Divisor	c_i	EIAV Uncertainty in %
Positioning	7.2.1	$-2.30\,\%$	R	1.73	1	$-1.33\,\%$
Mesh Resolution	7.2.2	$0.72\,\%$	N	1	1	$0.72\,\%$
Boundary Condition	7.2.3	$0.02\,\%$	N	1	1	$0.02\,\%$
Power Budget	7.2.4	*not appl.*	N	1	1	*not appl.*
Convergence	7.2.5	$0.53\,\%$	R	1.73	1	$0.31\,\%$
Phantom dielectrics	7.2.6	*not appl.*	R	1.73	1	*not appl.*
Combined Std. Uncertainty (k=1)						$1.54\,\%$

Table 11: Budget of the EIAV uncertainty contributions of the simulation parameters, analogue to the budget of the SAR uncertainty contributions of the simulation parameters to IEC/IEEE 62704-1 [6, Table 3]. Note: N, R, U = normal, rectangular, U-shaped probability distributions.

3.2.2 Model Related Uncertainty

For distances $d < \lambda/2$ the IEC/IEEE 62704-1 [6, section 7.3.3] states that *"[...] the only way to determine the uncertainty of the DUT model is by SAR measurements"*, which is not possible for the given frequency of the DUT. Therefore the procedure was modified by using the squared H-field values instead of SAR in [6, equation 14], similar to the assessment for distances $d \geq \lambda/2$ by [6, equation 13].

$$U_{\text{sim,DUT,SAR}} = max\left(\frac{|H^2_{\text{ref,n}} - H^2_{\text{sim,n}}|}{H^2_{\text{ref,max}}}\right) \tag{1}$$

$$= \left[\frac{|(1055.99\,\text{A/m})^2 - (1088.76\,\text{A/m})^2|}{(1055.99\,\text{A/m})^2}\right]_{z=8.50\,\text{mm}} \tag{2}$$

$$= 6.30\,\% \tag{3}$$

Thereby $z = 8.50\,\text{mm}$ is the location "n" where the maximum value of the expression occurs. For EIAV the RSS-102.NS.SIM [8, equation 1] requires that the uncertainty of the DUT model is calculated using H-field values instead of squared H-field values. This is due to the fact that EIAV is a field related quantity and not a power related quantity like SAR.

$$U_{\text{sim,DUT,EIAV}} = max\left(\frac{|H_{\text{ref,n}} - H_{\text{sim,n}}|}{H_{\text{ref,max}}}\right) \tag{4}$$

$$= \left[\frac{|1055.99\,\text{A/m} - 1088.76\,\text{A/m}|}{1055.99\,\text{A/m}}\right]_{z=8.50\,\text{mm}} \tag{5}$$

$$= 3.10\,\% \tag{6}$$

The customer stated an k=2 uncertainty of $1.33\,\text{dB} \Rightarrow 16.60\,\%$ for the measurements done by "cetecom advanced GmbH" (cf. section 1.4), so $8.30\,\%$ was used for the k=1 uncertainty of the measurement equipment and procedure. The phantom model itself does not contribute to the uncertainty because a homogeneous flat phantom was used.

Table 12 and 13 show the budgets of the uncertainty contributions of the model parameter and the combined model parameter related uncertainty.

Uncertainty Component (SAR)	Section in [6]	Tolerance in %	Probability Distribution	Divisor	c_i	Uncertainty in %
Uncertainty of the DUT model for SAR evaluation	7.3.2 or 7.3.3	6.30 %	N	1	1	6.30 %
Uncertainty of the phantom model	7.3.3	*not appl.*	N	1	1	*not appl.*
Uncertainty of the measurement equipment and procedure	-	8.30 %	N	1	1	8.30 %
Combined Std. Uncertainty (k=1)						10.42 %

Table 12: Budget of the uncertainty contributions of the model setup for 1g-SAR and 10g-SAR evaluation, corresponding to IEC/IEEE 62704-1 [6, Table 4]. Note: N, R, U = normal, rectangular, U-shaped probability distributions.

Uncertainty Component (EIAV)	Section in [6]	Tolerance in %	Probability Distribution	Divisor	c_i	Uncertainty in %
Uncertainty of the DUT model for EIAV evaluation	7.3.2 or 7.3.3	3.10 %	N	1	1	3.10 %
Uncertainty of the phantom model	7.3.3	*not appl.*	N	1	1	*not appl.*
Uncertainty of the measurement equipment and procedure	-	8.30 %	N	1	1	8.30 %
Combined Std. Uncertainty (k=1)						8.86 %

Table 13: Budget of the uncertainty contributions of the model setup for EIAV evaluation, corresponding to IEC/IEEE 62704-1 [6, Table 4]. Note: N, R, U = normal, rectangular, U-shaped probability distributions.

3.2.3 Model Validation

To validate the numerical model the equation 15 from IEC/IEEE 62704-1 [6, section 7.3.4] was calculated for the H-field line evaluation.

$$max\left(E_{\mathrm{n}}\right) = max\left(\sqrt{\frac{(\nu_{\mathrm{sim,n}} - \nu_{\mathrm{ref,n}})^2}{(\nu_{\mathrm{sim,n}} U_{\mathrm{sim,DUT,SAR(k=2)}})^2 + (\nu_{\mathrm{ref,n}} U_{\mathrm{ref(k=2)}})^2}}\right) \tag{7}$$

$$= max\left(\sqrt{\frac{(H^2_{\mathrm{sim,n}} - H^2_{\mathrm{ref,n}})^2}{(H^2_{\mathrm{sim,n}} U_{\mathrm{sim,DUT,SAR(k=2)}})^2 + (H^2_{\mathrm{ref,n}} U_{\mathrm{ref(k=2)}})^2}}\right) \tag{8}$$

$$= \left[\sqrt{\frac{((1006.14\,\mathrm{A/m})^2 - (975.39\,\mathrm{A/m})^2)^2}{((1006.14\,\mathrm{A/m})^2 \cdot 12.60\,\%)^2 + ((975.39\,\mathrm{A/m})^2 \cdot 16.60\,\%)^2}}\right]_{z=9.50\,\mathrm{mm}} \tag{9}$$

$$= 0.30 \leq 1 \tag{10}$$

Thereby $z = 9.50\,\mathrm{mm}$ is the location "n" where the maximum value of E_{n} occurs. For EIAV the model was validated using the DUT model uncertainty for EIAV evaluation and H-field values instead of squared H-field values.

$$max\left(E_{\mathrm{n}}\right) = max\left(\sqrt{\frac{(\nu_{\mathrm{sim,n}} - \nu_{\mathrm{ref,n}})^2}{(\nu_{\mathrm{sim,n}} U_{\mathrm{sim,DUT,EIAV(k=2)}})^2 + (\nu_{\mathrm{ref,n}} U_{\mathrm{ref(k=2)}})^2}}\right) \tag{11}$$

$$= max\left(\sqrt{\frac{(H_{\mathrm{sim,n}} - H_{\mathrm{ref,n}})^2}{(H_{\mathrm{sim,n}} U_{\mathrm{sim,DUT,EIAV(k=2)}})^2 + (H_{\mathrm{ref,n}} U_{\mathrm{ref(k=2)}})^2}}\right) \tag{12}$$

$$= \left[\sqrt{\frac{((1006.14\,\mathrm{A/m}) - (975.39\,\mathrm{A/m}))^2}{((1006.14\,\mathrm{A/m}) \cdot 6.21\,\%)^2 + ((975.39\,\mathrm{A/m}) \cdot 16.60\,\%)^2}}\right]_{z=9.50\,\mathrm{mm}} \tag{13}$$

$$= 0.18 \leq 1 \tag{14}$$

The condition/inequation is fulfilled for both SAR and EIAV, indicating that the deviation is within the expected uncertainty, and hence that the model is valid.

3.2.4 Uncertainty Budget

The budgets for simulation parameters related uncertainties and model related uncertainties were combined (k=1) and expanded (k=2) for 1g-SAR, 10g-SAR and EIAV as shown in table 14, 15 and 16 (see next page).

3.2.5 Uncertainty Penalty

The calculated Expanded Std. Uncertainties for SAR/EIAV do not exceed the maximum of 30 % stated in IEC/IEEE 62704-1 [6, Section 7.4]. Therefore uncertainty penalties as described in EN 62311 [10, Section 6.2, Equation 1] were not applied.

Uncertainty Component (1g-SAR)	Section in [6]	Tolerance in %	Probability Distribution	Divisor	c_i	Uncertainty in %
Uncertainty of the DUT model with respect to simulation parameters	7.2	2.41 %	N	1	1	2.41 %
Uncertainty of the developed numerical model of the DUT	7.3	10.42 %	N	1	1	10.42 %
Combined Std. Uncertainty (k=1)						10.70 %
Expanded Std. Uncertainty (k=2)						21.39 %

Table 14: Combined and expanded budget of the 1g-SAR uncertainty, corresponding to IEC/IEEE 62704-1 [6, Table 5]. Note: N, R, U = normal, rectangular, U-shaped probability distributions.

Uncertainty Component (10g-SAR)	Section in [6]	Tolerance in %	Probability Distribution	Divisor	c_i	Uncertainty in %
Uncertainty of the DUT model with respect to simulation parameters	7.2	2.26 %	N	1	1	2.26 %
Uncertainty of the developed numerical model of the DUT	7.3	10.42 %	N	1	1	10.42 %
Combined Std. Uncertainty (k=1)						10.66 %
Expanded Std. Uncertainty (k=2)						21.33 %

Table 15: Combined and expanded budget of the 10g-SAR uncertainty, corresponding to IEC/IEEE 62704-1 [6, Table 5]. Note: N, R, U = normal, rectangular, U-shaped probability distributions.

Uncertainty Component (EIAV)	Section in [6]	Tolerance in %	Probability Distribution	Divisor	c_i	Uncertainty in %
Uncertainty of the DUT model with respect to simulation parameters	7.2	1.54 %	N	1	1	1.54 %
Uncertainty of the developed numerical model of the DUT	7.3	8.86 %	N	1	1	8.86 %
Combined Std. Uncertainty (k=1)						8.99 %
Expanded Std. Uncertainty (k=2)						17.99 %

Table 16: Combined and expanded budget of the EIAV uncertainty, analogue to the budget of the SAR uncertainty from IEC/IEEE 62704-1 [6, Table 5]. Note: N, R, U = normal, rectangular, U-shaped probability distributions.

3.3 Additional Tests

3.3.1 Passive Receiver Impact

In the reported model the phantom is directly placed onto the air grid above the DUT. However, usually a WPT receiver such as a handset is placed on top of the DUT during charging operation. A receiver would increase the smallest possible approach distance, and its metal parts would act as a shield for the E- and H-fields, hence decreasing the exposure. To illustrate this effect, an additional simulation was done, whereby a passive phone receiver dummy was added to the model (cf. Figure 16).

Table 17 lists the maximum values for 1g-SAR, 10g-SAR and EIAV and their positions for model with the passive receiver dummy. As expected they are noticeable lower than in case of the reported model. The before mentioned shielding effect also qualitatively changes the SAR/EIAV distribution, as can be seen in Figure 17.

Quantity	Reported Model	With Passive Receiver
$SAR_{1g,\,max}$	$85.5499\,mW/kg$	$0.3382\,mW/kg$
$SAR_{10g,\,max}$	$41.3143\,mW/kg$	$0.1864\,mW/kg$
$EIAV_{unaveraged,max}$	$15.8422\,V/m$	$0.9387\,V/m$

Table 17: SAR and EIAV maximum values for the model with the passive receiver dummy.

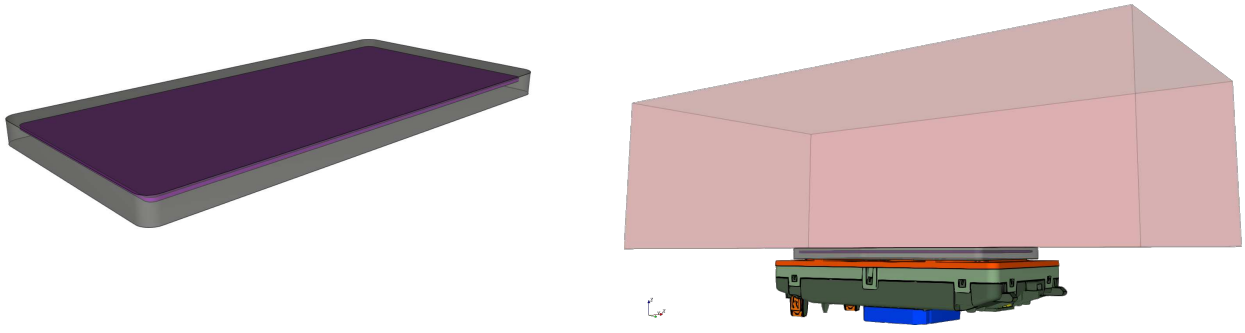

(a) (b)

Figure 16: Geometry of the passive receiver dummy, consisting of a $145 \cdot 70 \cdot 7\,mm$ dielectric housing with a metal plate inside (a). The receiver dummy was placed in between DUT and phantom (b).

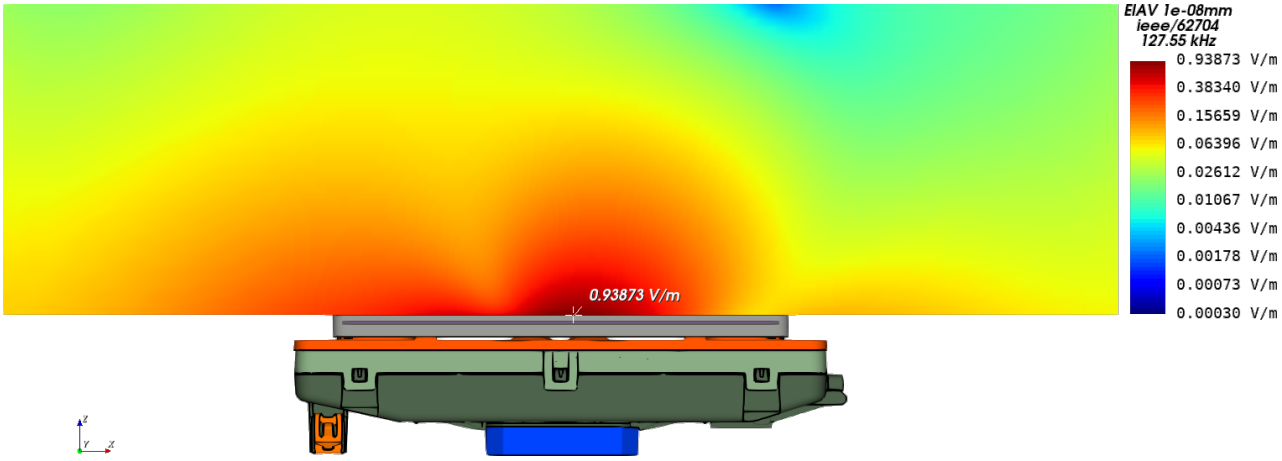

Figure 17: Cutplane through the maximum of the simulated EIAV inside the flat phantom for the model with the passive receiver dummy.

3.3.2 Field Behavior Across the Air-Phantom-Interface

Figure 18 depicts the behaviour of the E-field [3] and H-field across the air-phantom-interface ($z = 1.7\,\text{mm}$) of the reported model at the xy-location of the 1g-SAR maximum. The field behavior at the interface is as theoretically expected:

1. The tangential E-field components E_x and E_y are steady/continuous.
2. The normal E-field component E_z is discontinuous.
3. All H-field components are steady/continuous.
4. The H-field is practically unaffected (cf. Figure 18b vs. 19b) by the phantom, because of its low conductivity (cf. section 3).

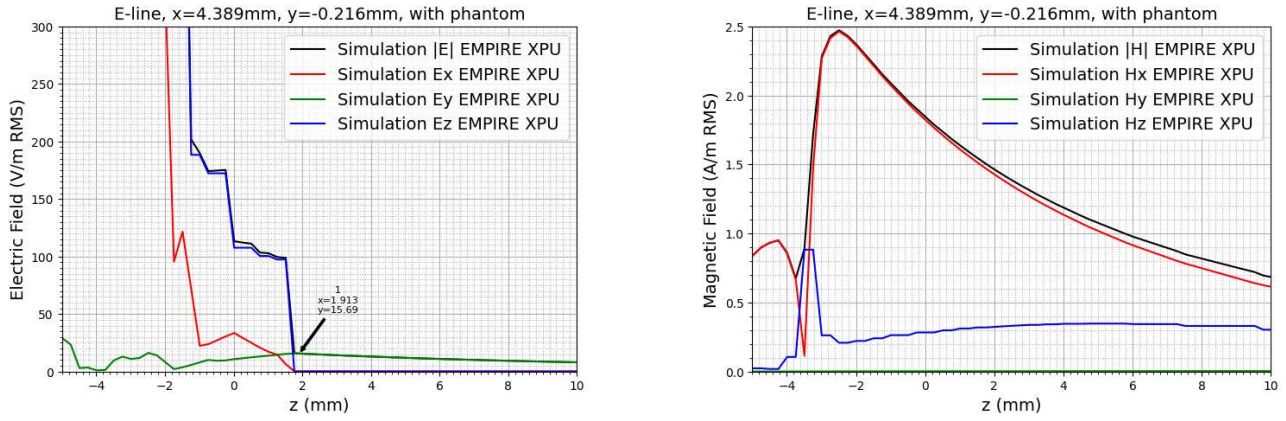

(a) (b)

Figure 18: Behavior of the E-field (a) and H-field (b) across the air-phantom-interface ($z = 0\,\text{mm}$) at the xy-location of the 1g-SAR maximum.

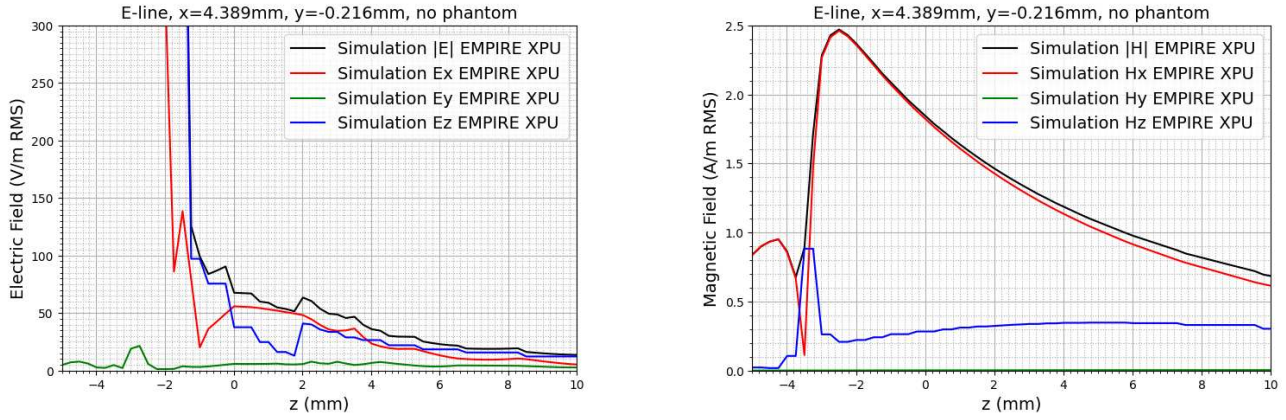

(a) (b)

Figure 19: E-field (a) and H-field (b) line plots analogue to Figure 18, but with no phantom present.

[3] It is very important to note that the simulated E-field distribution outside the phantom shown here only represents one possible physically correct distribution. Because the incident E-Field practically doesn't affect the exposure it was not validated and is hence presumably not the actual incident (!) E-Field distribution for the DUT.

3.3.3 Comparison Against Analytical Results

An additional check for the correctness of the numerical simulation results was done by replacing the large box shaped phantom (cf. section 3) with a small disc shaped phantom (cf. Figure 20). The disc has a height of 1 mm, a diameter of 6 mm and its axis equals the axis of the charging coil. The material properties of the disc phantom are the same as for the box shaped phantom.

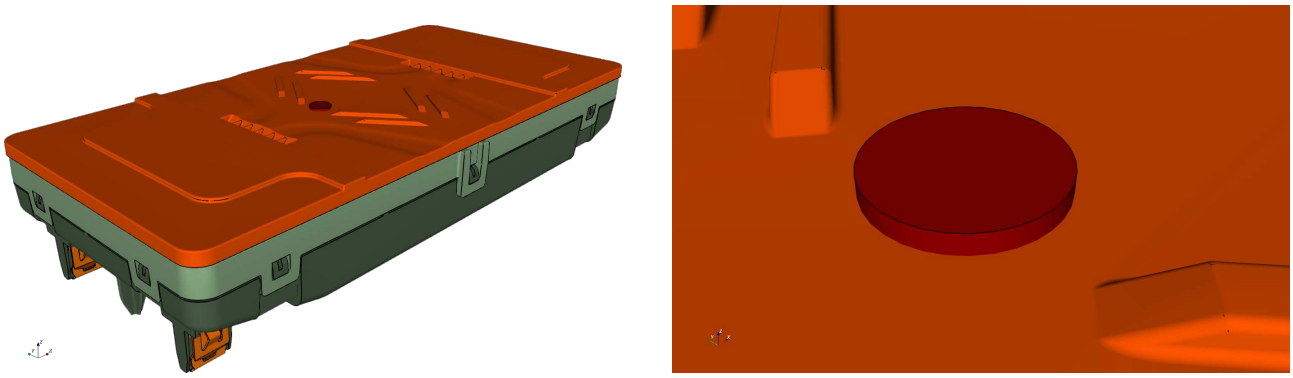

(a) (b)

Figure 20: Simulation geometry with the small disc shaped phantom.

Because the disc is small and its geometry is axial symmetric the internal E-field can be calculated analytically from the Maxwell-Faraday equation, considering the following conditions:

1. The H-field is approximately constant within the disc phantom: $\mathbf{H}(\mathbf{x}) = \mathbf{H}$
2. The H-field is oriented in z-direction within the disc phantom: $\mathbf{H}(\mathbf{x}) = H \cdot \mathbf{e}_z$
3. The internal E-field is axial symmetric and oriented in azimuthal direction: $\mathbf{E}(\mathbf{x}) = E_\phi(r) \cdot \mathbf{e}_\phi$
4. The internal E-field has therefore no radial- and no z-component: $E_r = E_z = 0$

$$\oint_{\partial A} \mathbf{E}(\mathbf{x},t) \cdot \mathrm{d}\mathbf{s} = -\frac{\mathrm{d}}{\mathrm{d}t} \iint_A \mathbf{B}(\mathbf{x},t) \cdot \mathrm{d}\mathbf{A} \tag{15}$$

$$\Rightarrow 2\pi r E_\phi(r,t) = -\frac{\mathrm{d}}{\mathrm{d}t} \pi r^2 \mu_0 H_z \cdot cos(\omega t) \tag{16}$$

$$\Leftrightarrow E_\phi(r,t) = -\frac{\mathrm{d}}{\mathrm{d}t} \frac{1}{2} r \mu_0 H_z \cdot cos(\omega t) \tag{17}$$

$$= -\frac{1}{2} r \mu_0 H_z \cdot \frac{\mathrm{d}}{\mathrm{d}t} \left(cos(\omega t)\right) \tag{18}$$

$$= -\frac{1}{2} r \mu_0 H_z \cdot (\omega \cdot -sin(\omega t)) \tag{19}$$

$$= -\frac{1}{2} r \mu_0 H_z \cdot (2\pi f \cdot -sin(\omega t)) \tag{20}$$

$$= r \mu_0 \pi f H_z \cdot sin(\omega t) \tag{21}$$

$$= E_\phi(r) \cdot sin(\omega t) \tag{22}$$

$$\Rightarrow E_\phi(r) = r \mu_0 \pi f H_z \tag{23}$$

Figure 21 shows the numerical simulation results of the internal E-field (EIAV) for the small disc phantom. The H-field within the disc phantom has values between $1760.91\,\mathrm{A/m}$ and $1801.12\,\mathrm{A/m}$.

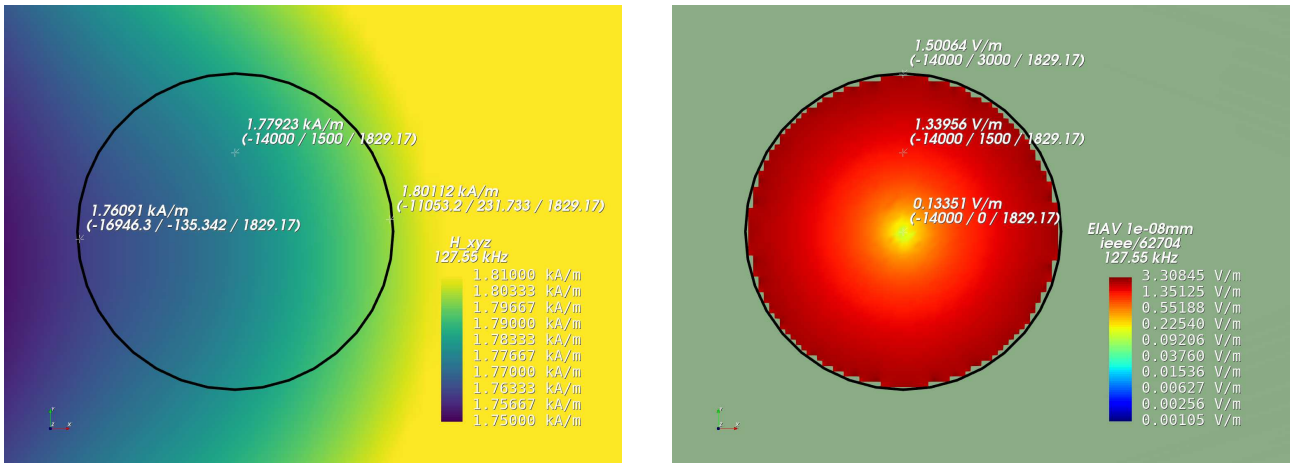

(a) (b)

Figure 21: H-field (a) and EIAV (b) within the small disc shaped phantom in the xy-plane for $z = 0.125\,\mathrm{mm}$.

At the position $x = 0\,\mathrm{mm}$ and $y = 1.5\,\mathrm{mm}$ the simulated H-field and EIAV within the disc phantom are:

$$H_{\mathrm{simul}}(r = y = 1.5\,\mathrm{mm}) = 1779.2\,\mathrm{A/m} \tag{24}$$
$$E_{\mathrm{simul}}(r = y = 1.5\,\mathrm{mm}) = 1.3396\,\mathrm{V/m} \tag{25}$$

The analytical internal E-field can be now calculated for the same position by inserting r, f and $H_z = H_{\mathrm{simul}}$ into equation (23):

$$E_{\mathrm{analytical}}(r = 1.5\,\mathrm{mm}) = E_{\phi,\mathrm{analytical}}(r = 1.5\,\mathrm{mm}) \tag{26}$$
$$= 1.5\,\mathrm{mm} \cdot \mu_0 \cdot \pi \cdot 127.55\,\mathrm{kHz} \cdot 1779.2\,\mathrm{A/m} \tag{27}$$
$$= 1.3439\,\mathrm{V/m} \tag{28}$$

The deviation of the simulation results from the analytical solution is therefore:

$$dev = \left| \frac{1.3396\,\mathrm{V/m} - 1.3439\,\mathrm{V/m}}{1.3439\,\mathrm{V/m}} \right| = 0.32\,\% \tag{29}$$

This demonstrates excellent agreement between simulation and analytical solution, considering the fact that the simulated H-field excited by the DUTs charging coil is not perfectly homogeneous within the disc phantom (cf. Figure 21a) as assumed for the analytical calculation. The comparison is supporting the results from the uncertainty analysis (cf. section 3.2) and the IEC/IEEE 62704-1 code verification [6, 7], indicating once again the accurate setup and simulation of the numerical DUT model.

3.4 Conclusion of the Evaluation

Summarizing the numerical exposure assessment of the DUT, the following can be stated:

1. The simulated magnetic field strength and the coil inductance are in agreement with the measurements (cf. section 2.2), indicating the accurate setup of the DUT simulation model (without phantom).
2. The investigated scenario (reported model) follows the worst-case assumption that:
   (a) The flat phantom is in direct contact with the DUT with no receiver in between.
   (b) The DUT is exciting its charging coil with the maximum expectable current, despite the fact that no receiver device is present.
   (c) The search mode duty cycle is neglected.
3. The model validation (cf. section 3.2.3) shows that in-equation 15 from IEC/IEEE 62704-1 is fulfilled, indicating a valid numerical model.
4. The uncertainty analysis returns Expanded Standard Uncertainties below the permissible 30% stated in IEC/IEEE 62704-1 section 7.4.
5. The evaluated maximum 1g-averaged SAR is $85.5499\,\mathrm{mW/kg}$.
6. The evaluated maximum 10g-averaged SAR is $41.3143\,\mathrm{mW/kg}$.
7. The evaluated maximum EIAV (internal Electric field, nerve stimulation) is $15.8422\,\mathrm{V/m}$.
8. The following interpretation of the assessment results (decision rule) is carried out on the basis of ILAC-G8:09/2019, chap. 4.2.1 according to the "Simple Acceptance" decision rule - as far as this is not contradicted by other normative requirements.
9. With respect to the statements above, the conclusion of this numerical exposure assessment report is, that the DUT does not exceed the SAR and/or EIAV exposure limits specified by ICNIRP [1], FCC [4], ISED [3] and EUCO [2]. A tabular evaluation can be found at the beginning of the report.

4 Appendix

4.1 Specific Information for Computational Modelling

FDTD algorithm implementation and validation: cf. [7]
Computing peak SAR from field components: cf. [7]
1g- and 10g-averaged SAR procedures: cf. [6, 7]
Processor type: AMD RYZEN THREADRIPPER 3970X 32-CORE PROCESSOR
Processor core usage: 32 cores
Memory usage: $507\,\mathrm{MB}$
Cell Size (min/max): $0.225\,\mathrm{mm}$ / $10.332\,\mathrm{mm}$
Domain Size: $660\,\mathrm{mm} \cdot 488\,\mathrm{mm} \cdot 416\,\mathrm{mm}$
Total amount of mesh cells: approx. $8.462\,\mathrm{MCells}$
Time step: $7.143190 \cdot 10^{-13}\,\mathrm{s}$
Total number of time steps: approx. $1.0\,\mathrm{MSteps}$
Simulation time: approx. 0hours and 15minutes and 27seconds
Simulation speed: $8837\,\mathrm{MCells/s}$
Excitation method: Gaussian pulse with $f_0 = 0\,\mathrm{Hz}$, $f_{\mathrm{BW}} = 50\,\mathrm{MHz}$
Phantom model implementation: cf. section 3
Tissue dielectric parameters: cf. section 3
Transmitter model implementation and validation: cf. section 2
Test device positioning: cf. section 3
Steady state termination procedures: A Gaussian pulse was used for the excitation and the simulation was terminated when the energy has dissipated to more than $-98.0\,\mathrm{dB}$.
Test results: cf. section 3

4.2 Abbreviations

Abbreviation	Description
CAD	Computer Aided Design
DUT	Device Under Test
EIAV	Averaged Internal Electric Field
EM	Electro Magnetic
FDTD	Finite Difference Time Domain
PCB	Printed Circuit Board
RF	Radio Frequency
RMS	Root Mean Square
SAR	Specific Absorption Rate
S/m	Siemens per meter $= 1/(\Omega m)$

4.3 Remarks

This report relates only to the item(s) evaluated. This report shall not be reproduced, except in its entirety, without the prior written approval of IMST GmbH. The results and statements contained in this report reflect the evaluation for the certain model described above. The manufacturer is responsible for ensuring that all production devices meet the intent of the requirements described in this report.

5 References

[1] International Commission on Non-Ionizing Radiation Protection (ICNIRP), "ICNIRP Guidelines for limitting Exposure to Electromagnetic Fields (100 KHz to 300 GHz)," 2020.

[2] European Council, "Council Recommendation of 12 July 1999 on the limitation of exposure of the general public to electromagnetic fields (0 Hz to 300 GHz), 1999/519/EC," July 1999.

[3] Innovation, Science and Economic Development Canada (ISED, Canada), "RSS-102 Issue 6 - Radio Frequency (RF) Exposure Compliance of Radiocommunication Apparatus (All Frequency Bands)," December 2023.

[4] Federal Communications Commission (FCC, USA), "FCC Limits for Specific Absorption Rate (SAR), 47 C.F.R. § 1.1310 and § 2.1093, 10–1–23 Edition," 2023.

[5] IMST GmbH. (2024, July) Empire XPU, Version 9.0.1. Carl-Friedrich-Gauß-Str. 2-4, 47475 Kamp-Lintfort, Germany. [Online]. Available: http://empire.de

[6] IEC/IEEE 62704-1:2017, "IEC/IEEE International Standard – Determining the peak spatial-average specific absorption rate (SAR) in the human body from wireless communications devices, 30 MHz to 6 GHz - Part 1: General requirements for using the finite-difference time-domain (FDTD) method for SAR calculations," pp. 1–86, 2017.

[7] IMST GmbH, "Empire XPU - Code Verification Report for IEC/IEEE 62704-1, Version 9.0.1," July 2024.

[8] Innovation, Science and Economic Development Canada (ISED, Canada), "RSS-102.NS.SIM Issue 1 - Simulation Procedure for Assessing Nerve Stimulation (NS) Compliance in Accordance with RSS-102," December 2023.

[9] IEC/IEEE 62209-1528:2020, "IEC/IEEE International Standard - Measurement procedure for the assessment of specific absorption rate of human exposure to radio frequency fields from hand-held and body-mounted wireless communication devices – Part 1528: Human models, instrumentation, and procedures (Frequency range of 4 MHz to 10 GHz)," pp. 1–284, 2020.

[10] CENELEC, "Assessment of electronic and electrical equipment related to human exposure restrictions for electromagnetic fields (0 Hz to 300 GHz), EN IEC 62311," January 2020.